Supplementary Materials

Dynamic phase-change metafilm absorber for strong designer modulation of visible light

Sun-Je Kim[1], Hansik Yun[1], Sungwook Choi[2], Jeong-Geun Yun[1], Kyungsoo Park[2], Sun Jae Jeong[2], Seung-Yeol Lee[3], Yohan Lee[1], Jangwoon Sung[1], Chulsoo Choi[1], Jongwoo Hong[1], Yong Wook Lee[2], and Byoungho Lee[1,*]

[1]Inter-University Semiconductor Research Center and School of Electrical and Computer Engineering, Seoul National University, Gwanakro 1, Gwanak-Gu, Seoul 08826, Republic of Korea
[2]Interdisciplinary Program of Biomedical Mechanical & Electrical Engineering and School of Electrical Engineering, Pukyong National University, Yongso-ro 45, Nam-Gu, Busan 48513, Republic of Korea
[3]School of Electronics Engineering, College of IT Engineering, Kyungpook National University, Daehakro 80, Buk-gu, Daegu 702-701, Republic of Korea
*E-mail: byoungho@snu.ac.kr

1. Comparison of optical properties of other phase-change materials

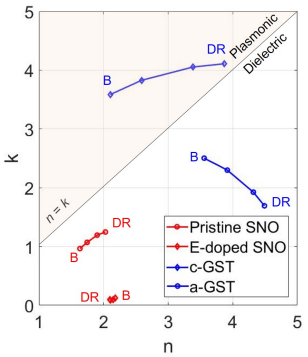

Figure S1. Complex refractive indices of $SmNiO_3$ (SNO) and $Ge_2Sb_2Te_5$ (GST) in the two distinct phases at the blue (473 nm), green (532 nm), red (633 nm), and deep red (700 nm) wavelengths. The figure shows that pristine SNO, c-GST, and a-GST have large extinction coefficients and complex refractive index coordinates near $n = k$ line. The (n, k) data of SNO is cited from the work by Li *et al*. [1] and GST data is measured by ellipsometry. The markings of B and DR denote the blue and deep red wavelengths, respectively.

2. Dynamic modulation of the Gires-Tournois VO_2 absorber

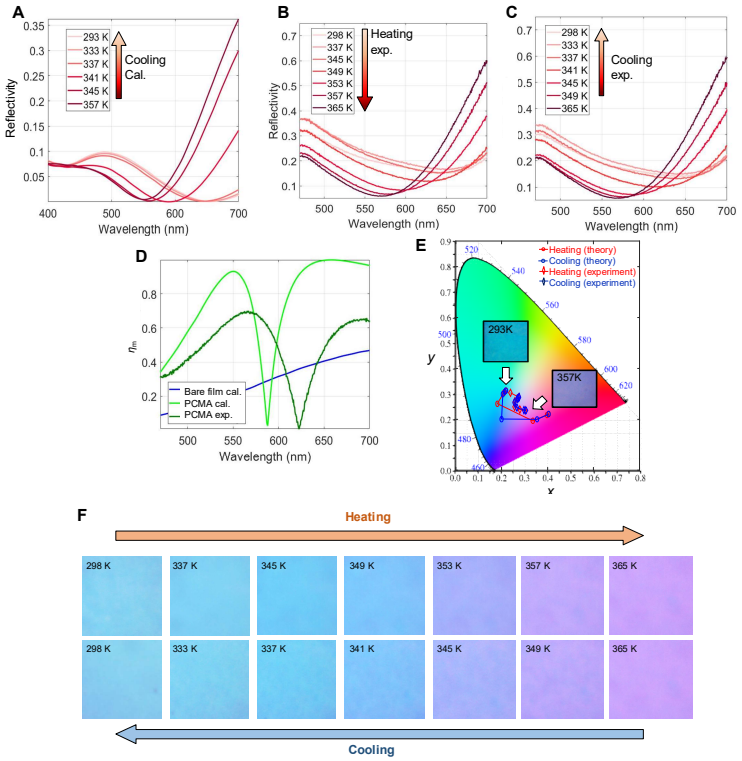

Figure S2 (A-C) Temperature-dependent gradual modulation of reflectance from the Gires-Tournois VO_2 absorber from (A) calculation and (B, C) measurement. (A) and (B, C) refer to data in processes of heating and cooling, respectively (D) Modulation depth of reflection intensity over broad bandwidth (E) Gradual active color tuning described by plotting in CIE space and (F) captured optical microscope image

3. Near-unity absorption conditions in Gires-Tournois VO_2 absorber: interference and thickness

The two distinguished destructive interferences occur in the Gires-Tournois VO_2 absorber with the two near-unity absorption resonances, D_i and D_m (the reflection dips at the insulating and metallic phases, respectively). The destructive interferences at the insulating and metallic phases are investigated theoretically with the dominant three lowest order complex partial reflection phasors. r_0, r_1, and r_2 denote the zeroth, first, and second order phasors at each resonance wavelength and phase of VO_2. r_i and r_m correspond to approximated total reflection phasors as sums of the three phasors at the insulating and metallic phases, respectively.

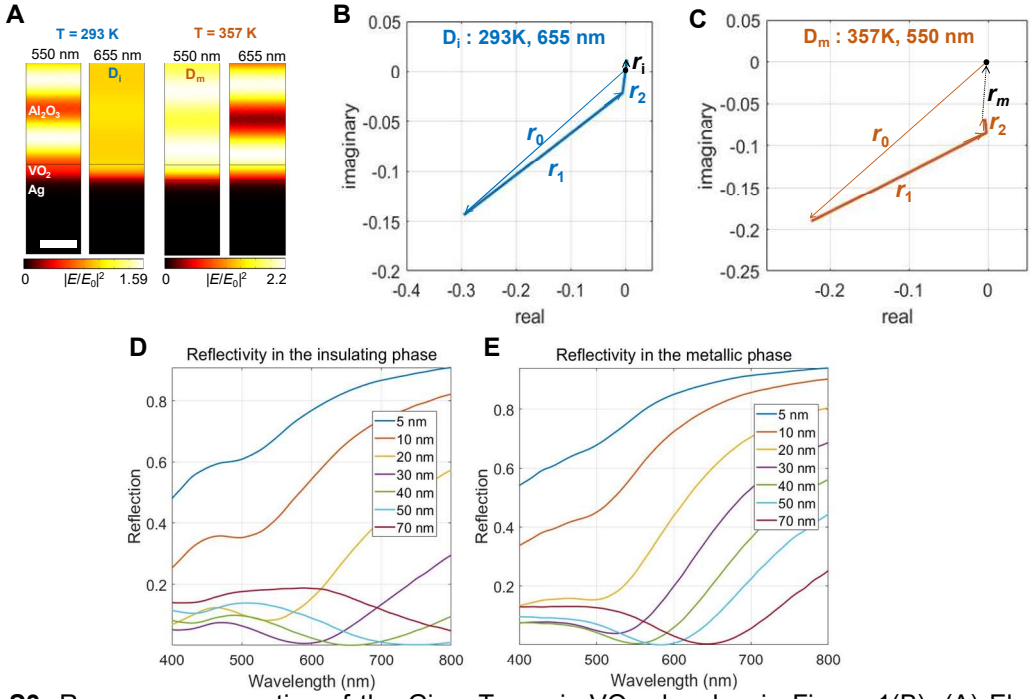

Figure S3. Resonance properties of the Gires-Tournois VO_2 absorber in Figure 1(B). (A) Electric field intensity profiles at the absorption resonances at the two VO_2 phases (B, C) Complex map describing the destructive interferences of dominant partial reflection phasors at the near-unity absorption dips of the Gires-Tournois VO_2 absorber structure. The interferences of the dominant three lowest order phasors at (b) room temperature and wavelength of 655 nm, (C) 357 K and wavelength of 550 nm, respectively. (D, E) Thickness-dependent reflectance spectra of the Gires-Tournois VO_2 absorber calculated by Fresnel-Airy's formula at the (D) insulating and (E) metallic phases, respectively. The legends denote thickness of the VO_2 layer.

4.Theoretical and numerical analysis on effective medium approximation in Ag-VO_2 metafilm absorber

Complex effective indices of the VO_2 metafilm absorbers with periodic inclusions of Ag nanobeams or nanodisks are analytically (A-D) and numerically (E, F) calculated. Moreover, the background colormap of reflectance shows corresponding reflectance values of the (n, k) coordinates. The thickness of VO_2 layer is fixed as 40 nm in common. As shown in Figs. S4E, 4F, 4H, embedding isotropic Ag nanodisk is not effective to achieve desirable considerable shift of resonance dip compared with anisotropic nanobeam type. Hence, we focused on studies of nanobeam type metafilms.

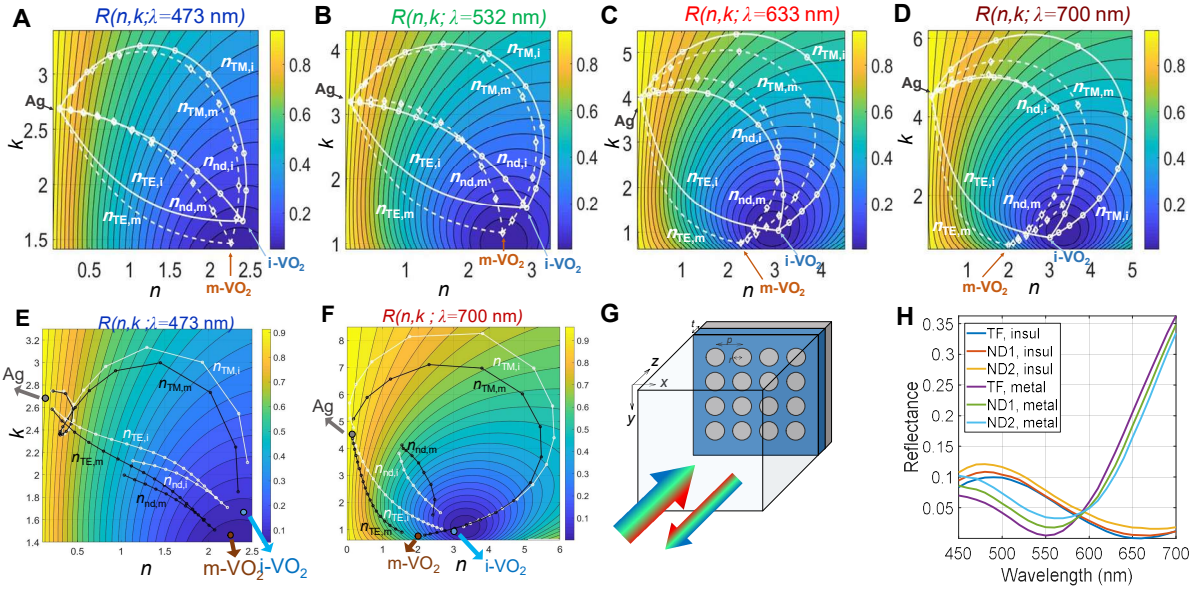

Figure S4. (A-D) The analytic Wiener's bounds and circular nanodisk (ND) type effective complex refractive indices with corresponding reflectance map in the (n, k) planes at the wavelengths of (A) 473 nm (Blue), (B) 532 nm (Green), (C) 633 nm (Red), (D) 700 nm (Deep red). Reflectance is calculated for the multilayer structure where a 40 nm-thick VO_2 layer is capped between Sapphire substrate and Ag mirror. f_{Ag} is varied from 0.05 and 0.95 at the effective index curves in (A-D). (E, F) Numerically retrieved Wiener's bounds and nanodisk type effective complex refractive indices at the (E) Blue (473 nm) and (F) Deep red (700 nm) colors. The background color map exhibits corresponding reflectance according (n, k) coordinate. TM, TE, nd, i, and m of marked indices near the curves denote TM polarization, TE polarization, nanodisk, insulating phase, and metallic phase, respectively. (E, F) In simulations of the ND type, f_{Ag} is varied from 0.05 and 0.45 at the effective index curves due to geometric limitation of a circle in a square. In cases of nanobeam type simulations, f_{Ag} is varied from 0.05 to 0.95. (G) Simulation schematic of the ND type metafilm absorber (p = 250 nm, t = 40 nm) and (H) numerically calculated tunable reflectance spectra for f_{Ag} = 0.17 and 0.23. TF in legend of (H) implies VO_2 thin film absorber without any Ag inclusions, and the ND1 and ND2 correspond to cases with f_{Ag} = 0.17 (r = 58 nm) and 0.23 (r = 67 nm), respectively.

5. Cross-sectional SEM images of the nanobeam type PCMA samples

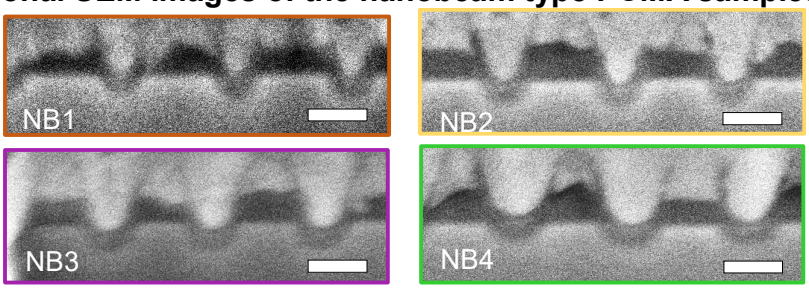

Figure S5. Focused ion beam-assisted cross-section SEM images of the fabricated NB1, NB2, NB3, and NB4. The NB2 cross-section image is also presented in Figure 1(D) of manuscript. The scale bars denote 100 nm.

6. Formulation of single port PCMA resonator using temporal coupled mode theory

Assuming time-dependence of $\exp(i\omega t)$, a single mode resonator with single port and low total decay rate ($\gamma_{tot} = \gamma_{abs} + \gamma_{rad}$) can be formulated with temporal coupled mode theory [4-8] as the following equations (S1-S3).

$$\frac{du}{dt} = (i\omega_0 - \gamma_{abs} - \gamma_{rad})u + ds_{1+}, \tag{S1}$$

$$s_{1-} = r_d s_{1+} + du, \tag{S2}$$

$$d^* d = |d|^2 \approx 2\gamma_{rad}. \tag{S3}$$

Here, $u, \omega_0, \gamma_{abs}, \gamma_{rad}, \text{and } d$ refer to complex amplitude of resonator mode, angular frequency of a resonance, internal loss-induced decay rate, external radiative decay rate, and coupling coefficient between a resonator and normal radiation mode (s_{1+}), respectively., while $|u|^2 = W$ is equal to the energy in the resonator. Equations (S2) and (S3) reveal the time-reversal property and energy conservation law assuming single port system approximation, respectively. As mentioned in the manuscript, total reflection (γ_{tot}) can be modelled as a sum of γ_d and γ_{id} . Here, γ_d can be theoretically calculated with the Airy's reflection formula of infinite series while $n_{eff} = \sqrt{\varepsilon_{vo2}(1-f_{Ag}) + \varepsilon_{Ag} f_{Ag}}$ for TE illumination and $n_{eff} = \sqrt{\left\{\varepsilon_{vo2}^{-1}(1-f_{Ag}) + \varepsilon_{Ag}^{-1} f_{Ag}\right\}^{-1}}$ for TM illumination, respectively. Resultantly, r_{tot} can be approximately formulated as the equation (S4). D is a positive-valued constant and φ is a real-valued constant.

$$r_{tot} = \frac{s_{1-}}{s_{1+}} \approx r_d + \frac{d^2}{i(\omega - \omega_0) + (\gamma_{abs} + \gamma_{rad})} \approx r_d + \frac{De^{i\varphi}}{i(\omega - \omega_0) + \gamma_{tot}}. \tag{S4}$$

7. Numerical fitting results of Fano-like resonator modelling

Based on the temporal coupled mode theory formulation of section 6, firstly, Lorentizan fitting of numerically calculated R_{id} from full field simulation is conducted for determination of $\omega_0, \gamma_{tot}, \varphi, \text{and } D$ based on the equation (S5) of numerical fitting function, $R_{id,fit}$.

$$R_{id,fit} = \left| r_{id,fit} \right|^2 = \frac{D^2}{\{(\omega - \omega_0)^2 + \gamma^2\}}. \quad \text{(S5)}$$

Using the fitted $\omega_0, \gamma_{tot}, \text{and } \varphi$ is calculated as the equation (S6).

$$\varphi = \angle r_{id,fit} + \tan^{-1}\left(\frac{\omega - \omega_0}{\gamma}\right) \quad \text{(S6)}$$

The tables S1 and S2 and Figure S6 present the fitted parameters of r_{id} of the NB1 and NB4 absorbers for TM and TE polarizations, respectively. As shown below and Figs. 5B and C, TM and TE cases of NB1 are well-fitted for both intensity and phase of r_{id} with properly determined parameters of $\omega_0, \gamma_{tot}, \varphi, \text{and } D$. However, the NB4 absorber cases with large f_{Ag} are not clearly fitted owing to blue shifts of resonances and lowered Q factors (Table S1 and Table S2). In case of the NB4 absorber, intensity of r_{id} is only fitted for TE case rather than TM case with break of single resonance modelling. Moreover, even the phase of r_{id} at TE case is not well fitted to constant value (Fig. S6C), while that of the NB1 absorber for both polarizations are approximately fitted to constants (Fig. S6A).

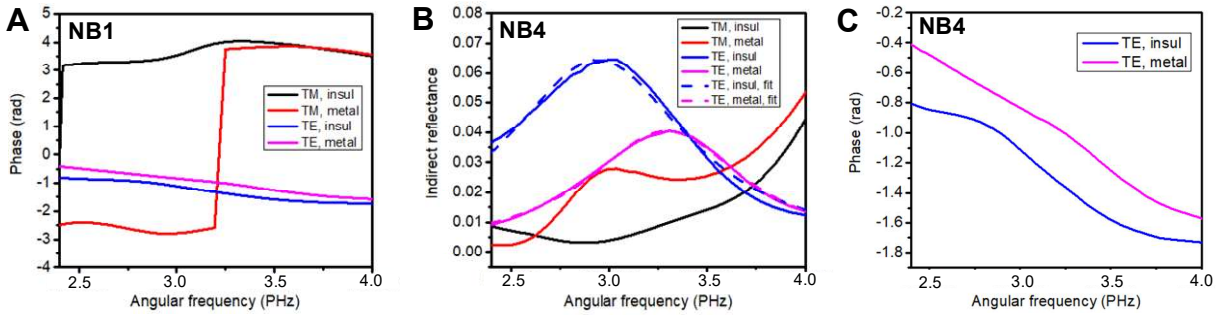

Figure S6. (A) Numerical extraction results of indirect reflection phase (φ) for TM and TE cases of the NB1 absorber at both phases of VO_2. (B) Indirect reflectance calculation of the NB4 absorber and numerical Lorentzian fitting of TE cases. (C) Numerical extraction results of indirect reflection phase (φ) for TE cases of the NB4 absorber at both phases of VO_2.

Table S1 Lorentzian oscillator fitting results of r_{id} for TM polarization

TM case	NB1 (f_{Ag} = 0.17)		NB4 (f_{Ag} = 0.4)	
	insulating	metallic	insulating	metallic
ω_0 (PHz·rad)	2.40127	3.03868	-	-
γ_{tot} (PHz)	0.32792	0.27636	-	-
D (THz)	20.737	21.561	-	-
φ (rad)	3	-2.5	-	-
$Q=\omega_0/(2\gamma_{tot})$	3.66137	5.49768	-	-

Table S2 Lorentzian oscillator fitting results of r_{id} for TE polarization

TE case	NB1 (f_{Ag} = 0.17)		NB4 (f_{Ag} = 0.4)	
	insulating	metallic	insulating	metallic
ω_0 (PHz·rad)	2.68642	3.0918	2.94197	3.29236
γ_{tot} (PHz)	0.54734	0.50305	0.56147	0.50310
D(THz)	72.89	52.20	142.54	101.16
φ (rad)	-1	-1	-	-
$Q=\omega_0/(2\gamma_{tot})$	2.45406	3.07305	2.61988	3.27207

8. Results on gradual modulation of the NB1 device

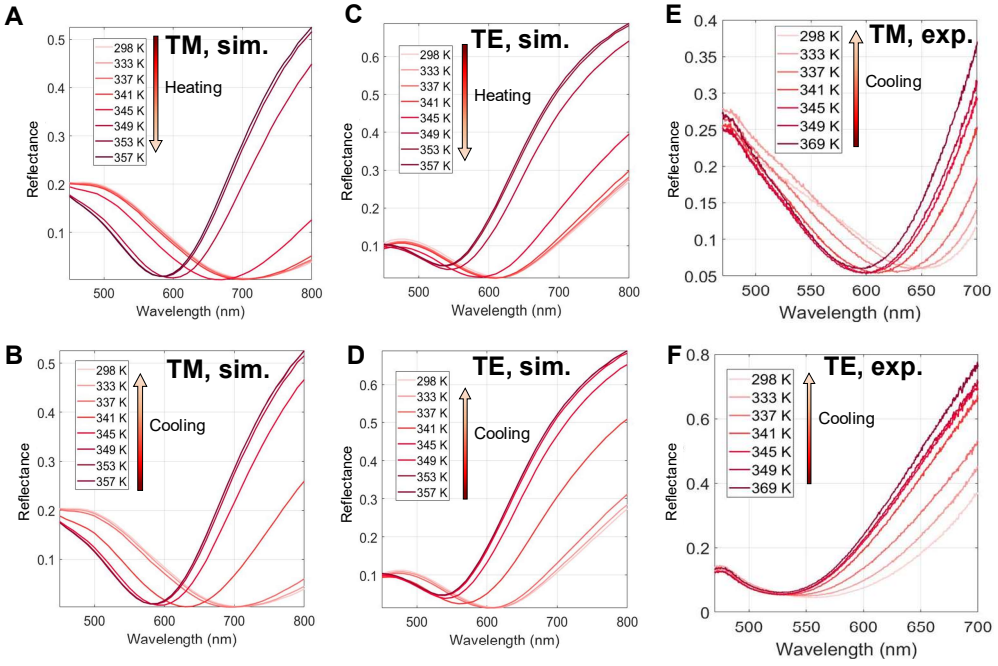

Figure S7. Gradual thermally-driven modulations of the NB1 PCMA. (A-D) simulation results for (A, B) TM and (C, D) TE polarizations, respectively. (A, C) and (B, D) correspond to heating and cooling induced modulations, respectively. (E, F) Experimental results in cooling process of the NB1 sample for (E) TM and (F) TE illuminations, respectively.

9. Thermally switchable anisotropic absorption dip of the NB1 sample

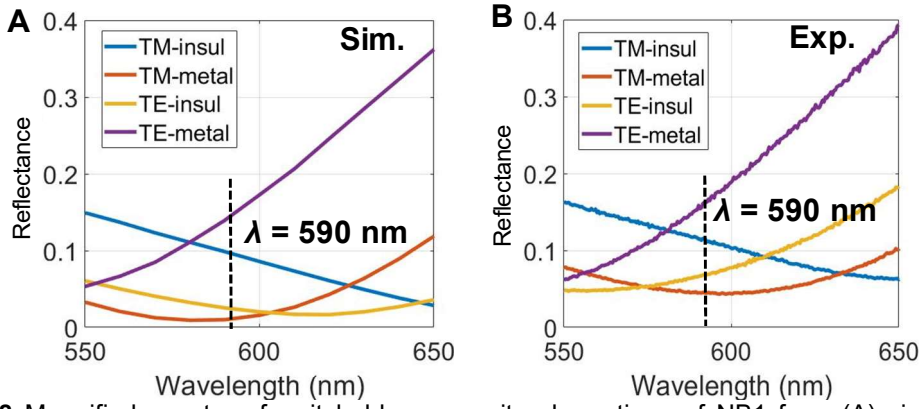

Figure S8 Magnified spectra of switchable near-unity absorptions of NB1 from (A) simulation and (B) experiment. At the wavelength of 590 nm, near-unity absorption is simultaneously achieved for TM illumination at the metalic phase and TE illumination at the insulating phase. This phenomenon induces the novel thermally driven tunable polarization filtering of the NB1 device.

10. Temperature-controlled ellipsometry and fitting

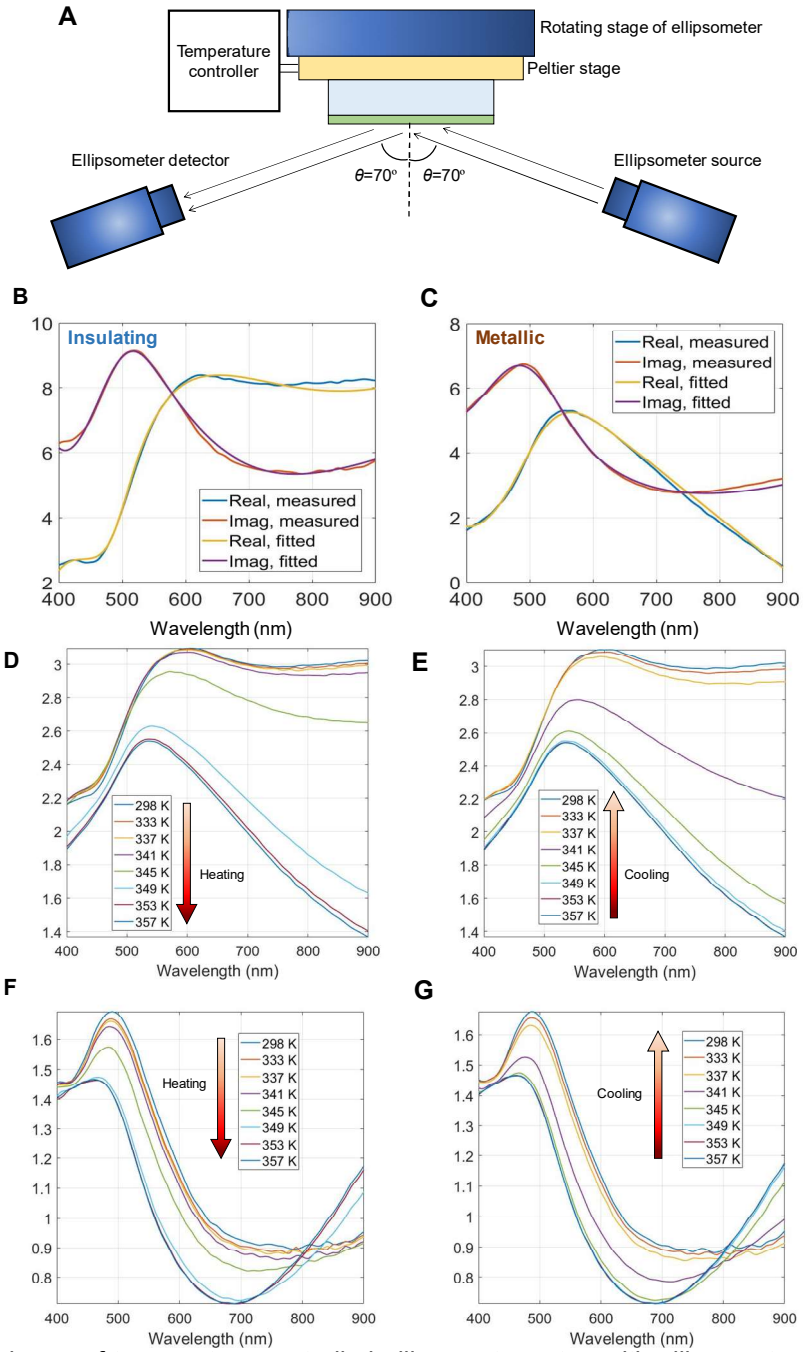

Figure S9. (A) Scheme of temperature-controlled ellipsometry setup with ellipsometer and Peltier stage. Measured and oscillator fitted dielectric functions at the (B) insulating and (C) metallic phases, respectively. (D) Heating and (E) cooling induced hysteric evolution of refractive indices. (F) and (G) correspond to heating and cooling induced hysteric evolution of extinction coefficients.

We performed spectroscopic ellipsometry in the visible and near-infrared regime for several temperatures between the room temperature (298 K) and 357 K. The measurement setup is described in the Figure S9A. Measured and oscillator fitted data of dielectric functions in the

insulating phase (298 K) and metallic phase (357 K) are suggested in the Figures S9B and C, respectively. The fitting method is based on the reference [9]. In the insulating phase, dielectric function is fitted to two Tauc-Lorentz oscillators

$$\varepsilon_2(E) = \frac{AE_nC(E-E_g)^2}{(E-E_n)^2+C^2E^2}\frac{1}{E}(E>E_g),\ 0\ (E<E_g), \tag{S8}$$

and the two Lorentz oscillators,

$$\varepsilon(E) = \frac{AB_rE_n}{E_n^2-E^2-iB_rE}. \tag{S9}$$

The fitted parameter sets of the Tauc-Lorentz oscillators are (A, E_n, C, E_g) = (80.104, 5.39392, 11.876, 1.6) and (-31.428, 2.7329, 0.82296, 1.4). The Lorentz oscillators are fitted with parameter sets, (A, E_n, B_r) = (4.8958, 1.158, 0.088137) and (14.381, 2.746, 1.2423).
On the other hand, in the metallic phase, oscillators are set to be the combination of a Drude oscillator, a Tauc-Lorentz oscillator, and a Lorentz oscillator. Drude oscillator is formulated as follows:

$$\varepsilon(E) = \frac{-AB_r}{E^2+iB_rE}. \tag{S10}$$

Parameter sets of the three oscillators are fitted as (A, B_r) = (30.974, 0.43764), (A, E_n, C, E_g) = (137.47, 2.7623, 39.464, 1.9813), and (A, E_n, B_r) = (5.0482, 2.5339, 1.1139), respectively.

11. VO_2 thin film properties

The electrical and surficial properties of a 40 nm-thick VO_2 film are verified with temperature controlled resistivity measurement and non-contact type atomic force microscopy.

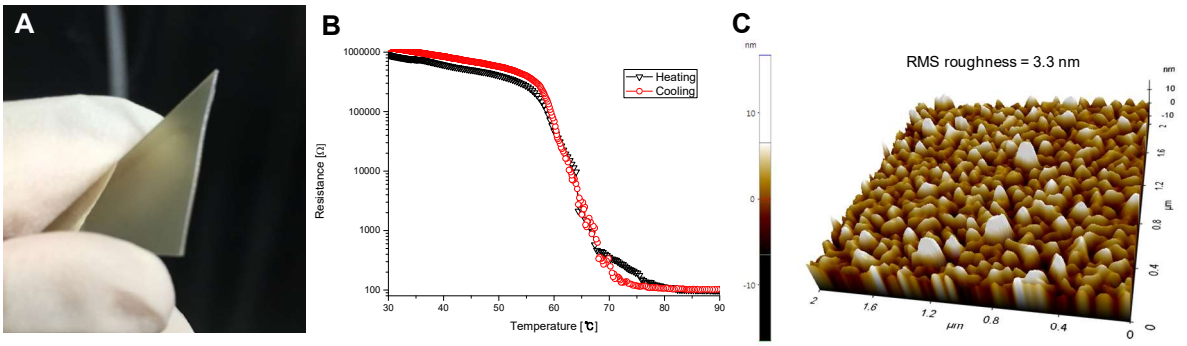

Figure S10. Characterization of a VO_2 film. (A) Camera image of a 40 nm-thick VO_2 film grown by PLD method (B) Phase-transition hysterisis curve of resistance via heating and cooling of a 40 nm-thick VO_2 film (C) 3D AFM surface image of a 40 nm-thick VO_2 film. RMS roughness is about 3.3 nm.

12. Measurement setup

We utilized temperature controlled Peltier stage, neutral white light emitting diode, and microscopic imaging spectrometer system to measure thermally tunable visible reflection spectra of the PCMAs.

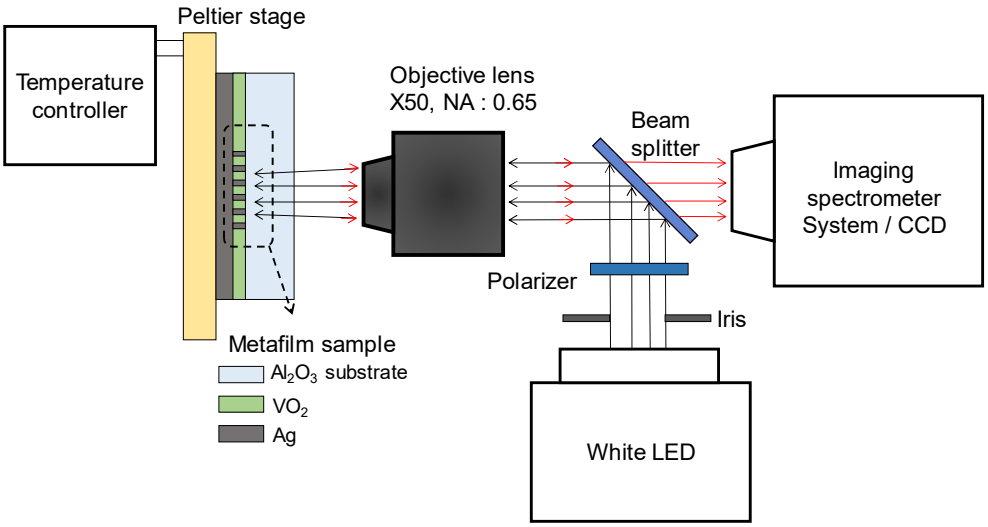

Figure S11. Scheme of temperature-controlled bright field back scattering spectroscopy

References (also cited in the manuscript)

[1] Li Z, Zhou Y, Qi H, Pan Q, Zhang Z, Shi NN, Lu M, Stein A, Li CY, Ramanathan S, Yu N. Correlated Perovskites as a New Platform for Super-Broadband-Tunable Photonics. Adv Mater 2016;28:9117-25.
[2] Fang A, Koschny T, Soukoulis CM. Optical anisotropic metamaterials: Negative refraction and focusing. Phys Rev B 2009;79:245127.
[3] Smith DR, Vier DC, Koschny T, Soukoulis CM. Electromagnetic parameter retrieval from inhomogeneous metamaterials. Phys. Rev. E 2005;71:036617.
[4] Haus HA. Waves and fields in optoelectronics, Prentice-Hall, 1984.
[5] Fan S, Suh W, Joannopoulos JD. Temporal coupled-mode theory for the Fano resonance in optical resonators. J Opt Soc Am A 2003;20:569-72.
[6] Wang X, Yu Z, Sandhu S, Fan S. Fundamental bounds on decay rates in asymmetric single-mode optical resonators. Opt Lett 2013;38:100-2.
[7] Yoon JW, Magnusson R. Fano resonance formula for lossy two-port systems. Opt Express 2013;21:17751-9.
[8] Cordaro A, Groep Jvd, Raza S, Pecora EF, Priolo F, Brongersma ML. Antireflection high-index metasurfaces combining Mie and Fabry-Pérot resonances. ACS Photonics 2019;6:453-9.
[9] Qazilbash MM, Schafgans AA, Burch KS, Yun SJ, Chae BG, Kim BJ, Kim HT, Basov DN. Electrodynamics of the vanadium oxides VO_2 and V_2O_3. Phys Rev B 2008;77:115121.